Three–dimensional dynamic simulation of elastocapillarity

Jesus Bueno · **Hugo Casquero** · **Yuri Bazilevs** · **Hector Gomez**

Abstract At small scales, the interaction of multicomponent fluids and solids can be dominated by capillary forces giving rise to elastocapillarity. Surface tension may deform or even collapse slender structures and thus, cause important damage in microelectromechanical systems. However, under control, elastocapillarity could be used as a fabrication technique for the design of new materials and structures. Here, we propose a computational model for elastocapillarity that couples nonlinear hyperelastic solids with two–component immiscible fluids described by the Navier–Stokes–Cahn–Hilliard equations. As fluid–structure interaction computational technique, we employ a boundary–fitted approach. For the spatial discretization of the problem we adopt a NURBS–based isogeometric analysis methodology. A strongly–coupled algorithm is proposed for the solution of the problem. The potential of this model is illustrated by solving several numerical examples, including, capillary origami, the static wetting of soft substrates, the deformation of micropillars and the three dimensional wrapping of a liquid droplet.

Keywords Elastocapillarity · Fluid–Structure Interaction (FSI) · Navier–Stokes–Cahn–Hilliard (NSCH) equations · Isogeometric Analysis (IGA) · Arbitrary Lagrangian–Eulerian (ALE) description

J. Bueno (*Corresponding Author*) - H. Casquero
Departamento de Métodos Matemáticos e de Representación,
Universidade da Coruña
Campus de Elviña, 15192, A Coruña, Spain
Tel.: +34-981-167000 Ext.: 5470
E-mail: jesus.bueno@udc.es

Y. Bazilevs
Department of Structural Engineering,
University of California, San Diego
9500 Gilman Drive, La Jolla, CA 92093, USA

H. Gomez
School of Mechanical Engineering,
Purdue University
585 Purdue Mall, West Lafayette, IN 47907, USA

1 Introduction

Multiphase and multicomponent flows have been widely studied [11,48] due to their importance in, e.g., mechanical, environmental and biomedical engineering. However, their mechanical interaction with solids has not received much attention until recently [36,49]. Understanding how these flows interact with solids is crucial to study, for example, cavitation–induced structural damage, phase–change–driven implosion and elastocapillarity. The phenomenon of elastocapillarity, whereby capillary forces at fluid–fluid interfaces deform solids, is particularly intriguing. Elastocapillarity [51,58], can be observed, for example, when water interacts with hair and other flexible fibers, which tend to assemble into bundles [9,29,28]. Another example can be found in our organism, where capillary forces may cause atelectasis [44], that is, the complete or partial collapse of the pulmonary alveoli. However, it is in micro and nanotechnologies, where the effect of elastocapillary forces is sparking greatest interest. Understanding elastocapillarity is essential for the design of new materials and devices at small scales. Capillary forces can damage microelectromechanical structures [50,63] and carbon nanotube carpets [21], but, under control, they can be used as a fabrication technique to deform straight pillars and build complex and robust 3D geometries at the micrometer and nanometer scales [25,65]. A numerical method capable of capturing the physics behind elastocapillary phenomena could become a useful tool for a better design of microfabricated products.

In the last decades, numerous efforts have been devoted to develop numerical methods for Fluid–Structure Interaction (FSI) problems. FSI methods may be classified into two

main groups, namely, boundary-fitted [6,53] and immersed approaches [15,19,42,75]. These methods have been applied to a large variety of problems such as, wind turbines [5, 35], heart valves [43,62], parachutes [55,60], and cell-scale blood flow [16,70] to name a few. However, most of the applications addressed up to now involve classical fluids. The interaction of complex fluids and solids has remained practically unexplored, although there has been recent works involving two–phase fluids [13,12]. In this paper, we propose a model for the interaction of two–component immiscible flows and hyperelastic structures. We use the model to study several elastocapillary problems, including, capillary origami [49], deformation of elastic micropillars [64] and static wetting of soft substrates [57].

Our computational method uses a boundary–fitted approach with a sharp fluid–solid interface. However, our approach to two–component immiscible flows is based on the Navier–Stokes–Cahn–Hilliard (NSCH) equations, which treat the fluid–fluid interface using a phase–field method. Phase–field approaches can be thought of as an alternative to sharp–interface methods in which interfaces are represented by thin transition regions. The key idea is to define an order parameter, or phase–field, that varies smoothly on the entire computational domain and acts as a marker for the location of the different phases. This notably simplifies the numerics compared to sharp–interface methods, although it implies the resolution of an additional equation for the evolution of the order parameter. This equation usually includes higher–order partial–differential operators that are stiff in space and time, and produce thin layers that evolve dynamically over the computational domain. Different strategies have been developed to deal with these computational challenges [31–33] allowing to use phase–field models for a wide range of applications such as, liquid-vapor transformations [14, 45], cancer growth [46,74], tumor angiogenesis [69,71], cell motility [52,47], and dendritic growth [40]. For a thorough discussion on phase-field models, see [34]. The NSCH equations can also be thought of as an extension of the incompressible Navier–Stokes equations to a multicomponent fluid with regularized surface tension. As a consequence, the NSCH model inherits the saddle point nature of the incompressible Navier-Stokes equations. This produces difficulties in the numerics that can be tackled using inf-sup stable discretizations, stabilized formulations or divergence-conforming bases.

In this work, we tackle the computational challenges associated with phase–field models by adopting Isogeometric Analysis (IGA) for the spatial discretization of the problem. IGA is a generalization of the finite element method that was proposed in [37]; see also [23]. IGA started using Non–Uniform Rational B–Splines (NURBS) as basis functions and, subsequently, was generalized to T–Splines (see, for example, [2,4,8,17,18]) and subdivision surfaces [73,72]. In the numerical examples presented here, we have used isoge-

ometric analysis based on NURBS, but our algorithms could be used in conjunction with other types of basis functions. To be able to use equal-order spaces for pressure and velocity in the fluid dynamics equations, we adopt a stabilized formulation for the NSCH equations based on the variational multiscale method (VMS). Regarding the time discretization, we use the generalized–α method [3,22,39].

2 Governing equations

2.1 Kinematics

Let us denote by $\widehat{\boldsymbol{x}}$ the coordinates of a reference domain $\Omega_{\widehat{\boldsymbol{x}}}$, which is fixed in time. We define a function $\widehat{\boldsymbol{\phi}}$ that maps the reference domain $\Omega_{\widehat{\boldsymbol{x}}}$ into its spatial configuration at time t, Ω_t, that is, $\widehat{\boldsymbol{\phi}} : \Omega_{\widehat{\boldsymbol{x}}} \times]0,T[\to \Omega_t$, where $]0,T[$ is the time interval of interest. We denote by $\boldsymbol{x}$ the coordinates in the spatial configuration, i.e., $\Omega_t \ni \boldsymbol{x} = \widehat{\boldsymbol{\phi}}(\widehat{\boldsymbol{x}},t)$. Using the mapping $\widehat{\boldsymbol{\phi}}$, we can define the displacement of a point in the referential domain $\widehat{\boldsymbol{u}}(\widehat{\boldsymbol{x}},t) = \widehat{\boldsymbol{\phi}}(\widehat{\boldsymbol{x}},t) - \widehat{\boldsymbol{x}}$, and its velocity $\widehat{\boldsymbol{v}} = \partial\widehat{\boldsymbol{\phi}}/\partial t$. Let us also define a material domain $\Omega_{\boldsymbol{X}}$ and the function $\boldsymbol{\phi} : \Omega_{\boldsymbol{X}} \times]0,T[\to \Omega_t$, which maps each material particle $\boldsymbol{X}$ into its spatial coordinate at time t, that is, $\boldsymbol{x} = \boldsymbol{\phi}(\boldsymbol{X},t)$. From the function $\boldsymbol{\phi}$, we can define the particle displacement $\boldsymbol{u}(\boldsymbol{X},t) = \boldsymbol{\phi}(\boldsymbol{X},t) - \boldsymbol{X}$, its velocity $\boldsymbol{v} = \partial\boldsymbol{\phi}/\partial t = \partial\boldsymbol{u}/\partial t$, and the deformation gradient $\boldsymbol{F} = \partial\boldsymbol{\phi}/\partial\boldsymbol{X}$.

In what follows, we will make use of the Eulerian counterpart of the particle velocity $\boldsymbol{v}$, namely, $\boldsymbol{v} \circ \boldsymbol{\phi}^{-1}$. However, in most cases, we will only use one symbol to denote a physical quantity. Furthermore, to avoid ambiguity in our notation we will use subscripts to clarify how derivatives should be understood. We will adopt the subscript $\boldsymbol{X}$ (respectively, $\widehat{\boldsymbol{x}}$) to indicate that the derivative is taken by holding $\boldsymbol{X}$ (respectively, $\widehat{\boldsymbol{x}}$) fixed. When no subscript is specified, the derivative is assumed to be taken by holding $\boldsymbol{x}$ fixed. For example, $\left.\dfrac{\partial\boldsymbol{v}}{\partial t}\right|_{\boldsymbol{X}}$ denotes the time derivative of the velocity holding $\boldsymbol{X}$ fixed.

2.2 Governing equations of fluid mechanics

In our model, the dynamics of the two–component fluid system is described by the Navier–Stokes–Cahn–Hilliard equations. The model describes the motion of two immiscible and incompressible fluids with matched density and viscosity. In the Eulerian frame, the equations can be written as

$$\nabla \cdot \boldsymbol{v} = 0, \tag{1a}$$

$$\rho \left(\frac{\partial \boldsymbol{v}}{\partial t} + \boldsymbol{v} \cdot \nabla \boldsymbol{v} \right) - \nabla \cdot \boldsymbol{\sigma}^f - \rho \boldsymbol{f} = 0, \tag{1b}$$

$$\frac{\partial \varphi}{\partial t} + \nabla \cdot (\varphi \boldsymbol{v}) - \nabla \cdot \left(M_\varphi \gamma_f \nabla \left(\frac{1}{\varepsilon} W'_\varphi - \varepsilon \Delta \varphi \right) \right) = 0, \tag{1c}$$

where ρ is the fluid density that we consider to be constant, $\boldsymbol{f}$ represents body forces per unit mass and $\varphi \in [-1, 1]$ is the phase–field variable. W_φ is a double–well potential, which we define as $W_\varphi = \left(\varphi^2 - 1 \right)^2 / 4$. The constant γ_f denotes the surface tension and ε is the interface thickness. M_φ represents the mobility, which is assumed to be constant for the examples presented herein. The fluid Cauchy stress tensor $\boldsymbol{\sigma}^f$ is given by $\boldsymbol{\sigma}^f = \boldsymbol{\tau} - p\boldsymbol{I} - \gamma_f \varepsilon \nabla \varphi \otimes \nabla \varphi$, where $\otimes$ denotes the usual vector outer product, p represents the pressure and $\boldsymbol{\tau}$ is the viscous stress tensor. For incompressible Newtonian fluids, $\boldsymbol{\tau}$ is defined as $\boldsymbol{\tau} = \bar{\mu} \left(\nabla \boldsymbol{v} + \nabla^T \boldsymbol{v} \right)$, where $\bar{\mu}$ is the viscosity coefficient, which is assumed to be constant. A complete derivation of Eqs. (1) from the sharp–interface theory may be found in [34].

2.3 Governing equations of solid mechanics

The behavior of the structure will be described by the momentum balance equation, which can be written in Lagrangian form as

$$\rho_0^s \frac{\partial^2 \boldsymbol{u}}{\partial t^2} \bigg|_X = \nabla_X \cdot \boldsymbol{P} + \rho_0^s \boldsymbol{f}^s. \tag{2}$$

Here, ρ_0^s is the mass density in the initial configuration, $\boldsymbol{P}$ denotes the first Piola–Kirchhoff stress tensor and $\boldsymbol{f}^s$ represents body forces per unit mass. To completely define the system, we adopt a nonlinear hyperelastic material as constitutive theory. In particular, we use the generalized neo–Hookean model with dilatational penalty proposed in [54]. In this model, the second Piola–Kirchhoff stress tensor is defined as

$$\boldsymbol{S} = \mu J^{-2/d} \left(\boldsymbol{I} - \frac{1}{d} \mathrm{tr}(\boldsymbol{C}) \boldsymbol{C}^{-1} \right) + \frac{\kappa}{2} \left(J^2 - 1 \right) \boldsymbol{C}^{-1}, \tag{3}$$

where κ and μ are the material bulk and shear moduli, which can be obtained from the Young modulus E and the Poisson ratio v^s using the relations $\kappa = E/(3(1 - 2v^s))$ and $\mu = E/(2(1 + v^s))$; $\boldsymbol{I}$ represents the identity tensor and d is the number of spatial dimensions; $\mathrm{tr}(\cdot)$ denotes the trace operator and J is the determinant of the deformation gradient, that is, $J = \det(\boldsymbol{F})$, where $\boldsymbol{F} = \boldsymbol{I} + \nabla_X \boldsymbol{u}$. Finally, $\boldsymbol{C}$ stands for the Cauchy–Green deformation tensor, i.e., $\boldsymbol{C} = \boldsymbol{F}^T \boldsymbol{F}$. From $\boldsymbol{S}$, the first Piola–Kirchhoff stress tensor can be computed by taking $\boldsymbol{P} = \boldsymbol{F}\boldsymbol{S}$. Let us also define the solid Cauchy stress tensor $\boldsymbol{\sigma}^s = J^{-1} \boldsymbol{F}\boldsymbol{S}\boldsymbol{F}^T = J^{-1} \boldsymbol{P}\boldsymbol{F}^T$.

3 Numerical formulation

3.1 Computational framework

We adopt a boundary–fitted technique with matching discretization at the fluid–structure interface. This choice permits to strongly impose kinematic boundary conditions at the fluid-solid interface and results in more accurate solutions at the fluid–solid interface as long as the mesh does not undergo large distortions. We use the Lagrangian description to derive the semi–discrete form of the solid equations and the Arbitrary Lagrangian–Eulerian (ALE) description [26,27,38] for the fluid domain. This means that the fluid mesh needs to be updated to accommodate the motion of the structure. For this purpose, we solve an additional linear elasticity problem subject to displacement boundary conditions coming from the motion of the solid. In ALE approaches, the partial time derivatives in the governing equations are taken by holding $\widehat{\boldsymbol{x}}$ fixed while the space derivatives are taken with respect to $\boldsymbol{x}$. This particularity enables to use semi–discrete methods, even when the equations are posed on a moving domain [3]. The ALE form of the NSCH equations can be derived using the techniques presented in [6, 27]. This leads to the system

$$\nabla \cdot \boldsymbol{v} = 0, \tag{4a}$$

$$\rho \left(\frac{\partial \boldsymbol{v}}{\partial t} \bigg|_{\widehat{x}} + (\boldsymbol{v} - \widehat{\boldsymbol{v}}) \cdot \nabla \boldsymbol{v} \right) - \nabla \cdot \boldsymbol{\sigma}^f - \rho \boldsymbol{f} = 0, \tag{4b}$$

$$\frac{\partial \varphi}{\partial t} \bigg|_{\widehat{x}} + (\boldsymbol{v} - \widehat{\boldsymbol{v}}) \cdot \nabla \varphi - \nabla \cdot \left(M_\varphi \gamma_f \nabla \left(\frac{1}{\varepsilon} W'_\varphi - \varepsilon \Delta \varphi \right) \right) = 0, \tag{4c}$$

where $\widehat{\boldsymbol{v}}$ is the velocity of the fluid domain [3].

Remark Another boundary–fitted approach that could be adopted as alternative to ALE methods is the space–time technique. This would allow to discretize directly the Eulerian form of the NSCH equations; see [6,7,59,61] for recent advances in space–time methods.

3.2 Computational domain

We will denote by Ω_0 the initial configuration of the fluid and solid domains combined, that is, $\Omega_0 = \overline{\Omega_0^f \cup \Omega_0^s}$, with $\Omega_0^f \cap \Omega_0^s = \emptyset$, where superscripts s and f refer to the solid and the fluid domain, respectively. Ω_0 is adopted as the material and reference configuration. The spatial configuration of Ω_0 at time t is designated as Ω_t, and can also be decomposed as $\Omega_t = \overline{\Omega_t^f \cup \Omega_t^s}$, with $\Omega_t^f \cap \Omega_t^s = \emptyset$. Let us also denote by Γ_0 and Γ_t the fluid–solid interface at the initial and the current configuration, respectively. Γ_0^s and Γ_t^s (Γ_0^f and Γ_t^f) will refer to the boundary of the solid (fluid) domain without the part of the fluid–structure interface.

3.3 Continuous problem in the weak form

3.3.1 Fluid mechanics

In the fluid mechanics problem we focus on solid–wall boundary conditions, by setting the velocity to a given value. Additionally, and with the purpose of attaining well–posedness in the NSCH system, we enforce the following boundary conditions on the phase–field variable,

$$\nabla \varphi \cdot \boldsymbol{n}^f = |\nabla \varphi| \cos(\theta_c) \qquad \text{on} \quad \Gamma_t, \tag{5a}$$

$$\nabla \varphi \cdot \boldsymbol{n}^f = 0 \qquad \text{on} \quad \Gamma_t^f, \tag{5b}$$

and

$$M_\varphi \gamma_f \nabla \left(\frac{1}{\varepsilon} W_\varphi' - \varepsilon \Delta \varphi \right) \cdot \boldsymbol{n}^f = 0 \quad \text{on} \quad \Gamma_t^f \cup \Gamma_t, \tag{6}$$

where $\boldsymbol{n}^f$ is the unit outward normal to the fluid boundary and θ_c denotes the contact angle between the fluid–fluid interface and the solid, measured in the phase of value $\varphi = 1$. The imposition of boundary condition (5) can be notably simplified by introducing in our problem a new variable $\Upsilon = \Delta \varphi$. This implies that the phase–field equation (4c) is split into two lower–order equations, allowing to use the classical finite element method for the spatial discretization of the problem.

In preparation for the spatial discretization of the fluid dynamics problem, we derive a weak form of Eqs. (4). Let $L^2(\Omega_t^f)$ be the space of scalar–valued functions that are square–integrable on Ω_t^f. We define the trial function space for the pressure variable as

$$\mathscr{X}^p = \left\{ p \mid p \in L^2\left(\Omega_t^f\right), \int_{\Omega_t^f} p \, \mathrm{d}\Omega_t^f = 0 \right\}. \tag{7}$$

The weighting function space for the pressure variable $\mathscr{Y}^p$ will be indentical to $\mathscr{X}^p$. The trial solution spaces for Υ and φ are denoted by $\mathscr{X}^\Upsilon$ and $\mathscr{X}^\varphi$, respectively. We take $\mathscr{X}^\Upsilon = \mathscr{X}^\varphi = H^1(\Omega_t^f)$, where $H^1(\Omega_t^f)$ is the Sobolev space of square–integrable functions with square–integrable first derivatives. The weighting function spaces for Υ and φ are identical to their corresponding trial solution spaces. The trial solution space $\mathscr{X}^v$ for $\boldsymbol{v}$ is also a subset of $H^1(\Omega_t^f)$ whose members satisfy all Dirichlet boundary conditions. The weighting function space $\mathscr{Y}^v$ is identical to $\mathscr{X}^v$, but all restrictions on the Dirichlet boundary are homogeneous. With the above considerations, the variational formulation of the fluid mechanics problem may be stated as follows: Find $p \in \mathscr{X}^p$, $\boldsymbol{v} \in \mathscr{X}^v$, $\varphi \in \mathscr{X}^\varphi$ and $\Upsilon \in \mathscr{X}^\Upsilon$ such that $\forall w^1 \in \mathscr{Y}^p$, $\boldsymbol{w}^2 \in \mathscr{Y}^v$, $w^3 \in \mathscr{Y}^\varphi$ and $w^4 \in \mathscr{Y}^\Upsilon$,

$$B^f(w^1, \boldsymbol{w}^2, w^3, w^4, p, \boldsymbol{v}, \varphi, \Upsilon; \widehat{\boldsymbol{v}}) = F^f(\boldsymbol{w}^2). \tag{8}$$

where

$$B^f(w^1, \boldsymbol{w}^2, w^3, w^4, p, \boldsymbol{v}, \varphi, \Upsilon; \widehat{\boldsymbol{v}}) =$$

$$\int_{\Omega_t^f} w^1 \nabla \cdot \boldsymbol{v} \mathrm{d}\Omega_t^f + \int_{\Omega_t^f} \boldsymbol{w}^2 \cdot \rho \left(\left. \frac{\partial \boldsymbol{v}}{\partial t} \right|_{\widehat{x}} + (\boldsymbol{v} - \widehat{\boldsymbol{v}}) \cdot \nabla \boldsymbol{v} \right) \mathrm{d}\Omega_t^f$$

$$+ \int_{\Omega_t^f} \nabla \boldsymbol{w}^2 : \boldsymbol{\sigma}^f \mathrm{d}\Omega_t^f + \int_{\Omega_t^f} w^3 \left(\left. \frac{\partial \varphi}{\partial t} \right|_{\widehat{x}} + (\boldsymbol{v} - \widehat{\boldsymbol{v}}) \cdot \nabla \varphi \right) \mathrm{d}\Omega_t^f$$

$$+ \int_{\Omega_t^f} \nabla w^3 \cdot M_\varphi \gamma_f \nabla \left(\frac{1}{\varepsilon} W_\varphi' - \varepsilon \Upsilon \right) \mathrm{d}\Omega_t^f$$

$$+ \int_{\Omega_t^f} w^4 \Upsilon \mathrm{d}\Omega_t^f + \int_{\Omega_t^f} \nabla w^4 \cdot \nabla \varphi \mathrm{d}\Omega_t^f$$

$$- \int_{\Gamma_t} w^4 |\nabla \varphi| \cos(\theta_c) \mathrm{d}\Gamma_t, \tag{9}$$

and

$$F^f(\boldsymbol{w}^2) = \int_{\Omega_t^f} \boldsymbol{w}^2 \cdot \rho \, \boldsymbol{f} \mathrm{d}\Omega_t^f. \tag{10}$$

Note that the variational formulation (8)–(10) weakly imposes the NSCH equations and the boundary conditions (5) and (6). If Dirichlet boundary conditions are not set on the entire boundary for velocity, then the variational formulation weakly imposes the conjugate stress–free condition on that part of the boundary.

In order to stabilize the NSCH equations, we make use of the VMS method and split the weighting and the trial solution spaces corresponding to pressure and velocity into a coarse and a fine scale subspaces, that is, $\mathscr{X}^p = \mathscr{X}_g^p \oplus \mathscr{X}_q^p$, $\mathscr{X}^v = \mathscr{X}_g^v \oplus \mathscr{X}_q^v$, $\mathscr{Y}^p = \mathscr{Y}_g^p \oplus \mathscr{Y}_q^p$ and $\mathscr{Y}^v = \mathscr{Y}_g^p \oplus \mathscr{Y}_q^v$. Here, the subscripts g and q denote the coarse and the fine scales, respectively. This implies that p, $\boldsymbol{v}$, w^1 and $\boldsymbol{w}^2$ may be written as

$$p = p_g + p_q, \tag{11a}$$

$$w^1 = w_g^1 + w_q^1, \tag{11b}$$

$$\boldsymbol{v} = \boldsymbol{v}_g + \boldsymbol{v}_q, \tag{11c}$$

$$\boldsymbol{w}^2 = \boldsymbol{w}_g^2 + \boldsymbol{w}_q^2. \tag{11d}$$

3.3.2 Solid mechanics

In order to define suitable boundary conditions for the solid mechanics problem, we assume that the solid boundary Γ_0^s can be decomposed into Dirichlet and Neumann parts, which will be designated as $(\Gamma_0^s)_D$ and $(\Gamma_0^s)_N$, respectively. We denote by $\mathscr{X}^s = \mathscr{X}^s(\Omega_0^s)$ a trial function space whose members satisfy all Dirichlet boundary conditions. $\mathscr{Y}^s = \mathscr{Y}^s(\Omega_0^s)$ is a weighting function space identical to $\mathscr{X}^s$, which verifies homogeneous conditions on $(\Gamma_0^s)_D$. The trial and weighting function spaces are subsets of $H^1(\Omega_0^s)$. The variational formulation of the solid mechanics problem may be stated as follows: Find $\boldsymbol{u} \in \mathscr{X}^s$ such that $\forall \boldsymbol{w}^s \in \mathscr{Y}^s$,

$$B^s(\boldsymbol{w}^s, \boldsymbol{u}) = F^s(\boldsymbol{w}^s), \tag{12}$$

where

$$B^s(\boldsymbol{w}^s, \boldsymbol{u}) = \int_{\Omega_0^s} \left(\boldsymbol{w}^s \cdot \rho_0^s \frac{\partial^2 \boldsymbol{u}}{\partial t^2} \bigg|_X + \nabla_X \boldsymbol{w}^s : \boldsymbol{P} \right) d\Omega_0^s \qquad (13)$$

and

$$F^s(\boldsymbol{w}^s) = \int_{\Omega_0^s} \boldsymbol{w}^s \cdot \rho_0^s \boldsymbol{f}^s d\Omega_0^s + \int_{(\Gamma_0^s)_N} \boldsymbol{w}^s \cdot \widehat{\boldsymbol{h}} d(\Gamma_0^s)_N. \qquad (14)$$

The previous variational formulation weakly enforces the Neumman boundary condition $\boldsymbol{P}\widehat{\boldsymbol{n}}^s = \widehat{\boldsymbol{h}}$ on $(\Gamma_0^s)_N$, where $\widehat{\boldsymbol{n}}^s$ represents the unit outward normal to the solid boundary in the material domain and $\widehat{\boldsymbol{h}}$ is a given traction.

3.3.3 Mesh motion

As the solid deforms, the fluid domain needs to be updated to accommodate to the fluid–structure interface motion. With this purpose, we solve a succession of fictitious linear elastic boundary–value problems [3,41,56,66–68], using as boundary conditions the displacement data on the fluid–solid interface. The fluid domain motion will be associated to the mapping $\widehat{\boldsymbol{\phi}}$. Let us define the displacement of the reference domain at time t as

$$\widehat{\boldsymbol{u}}_t(\widehat{\boldsymbol{x}}) = \widehat{\boldsymbol{u}}(\widehat{\boldsymbol{x}},t) = \widehat{\boldsymbol{\phi}}_t(\widehat{\boldsymbol{x}}) - \widehat{\boldsymbol{x}}. \qquad (15)$$

where $\widehat{\boldsymbol{\phi}}_t(\widehat{\boldsymbol{x}}) = \widehat{\boldsymbol{\phi}}(\widehat{\boldsymbol{x}},t)$. To determine $\widehat{\boldsymbol{\phi}}_t$, and thus, the motion of the fluid domain, we use the identity

$$\widehat{\boldsymbol{\phi}}_t(\widehat{\boldsymbol{x}}) = \widehat{\boldsymbol{\phi}}_{\tilde{t}}(\widehat{\boldsymbol{x}}) + (\widehat{\boldsymbol{u}}_t - \widehat{\boldsymbol{u}}_{\tilde{t}})(\widehat{\boldsymbol{x}}), \qquad (16)$$

where $\widehat{\boldsymbol{u}}_t - \widehat{\boldsymbol{u}}_{\tilde{t}}$ is obtained from a linear elastic boundary–value problem. Here, $\tilde{t} < t$ is a time instant close to t. In general, in our problems $\tilde{t}$ is the final configuration of the previous time step.

Let us define $\boldsymbol{u}^m$ as $\boldsymbol{u}^m = \widehat{\boldsymbol{u}}_t - \widehat{\boldsymbol{u}}_{\tilde{t}}$. $\boldsymbol{u}^m$ is obtained by solving fictitious linear–elastic boundary value problems, subject to the Dirichlet boundary conditions $\boldsymbol{u}^m = \boldsymbol{u}_t \circ \boldsymbol{\phi}_t^{-1} - \boldsymbol{u}_{\tilde{t}} \circ \boldsymbol{\phi}_{\tilde{t}}^{-1}$ on $\Gamma_{\tilde{t}}$, where $\boldsymbol{u}_t$ and $\boldsymbol{u}_{\tilde{t}}$ are the particle displacement at times t and $\tilde{t}$, respectively. These Dirichlet boundary conditions are strongly built into the trial solution space $\mathscr{V}^m = \mathscr{V}^m(\Omega_{\tilde{t}}^f)$, which is a subset of $H^1(\Omega_{\tilde{t}}^f)$. $\mathscr{W}^m = \mathscr{W}^m(\Omega_{\tilde{t}}^f)$ is a weighting function space identical to $\mathscr{V}^m$ except that it satisfies homogeneous conditions on the boundary. The variational formulation of the fluid domain motion can be stated as follows: Find $\boldsymbol{u}^m \in \mathscr{V}^m$ such that $\forall \boldsymbol{w}^m \in \mathscr{W}^m$,

$$B^m(\boldsymbol{w}^m, \boldsymbol{u}^m) = 0, \qquad (17)$$

where

$$B^m(\boldsymbol{w}^m, \boldsymbol{u}^m) = \int_{\Omega_{\tilde{t}}^f} \nabla_{\tilde{x}}^{sym} \boldsymbol{w}^m : 2\mu^m \nabla_{\tilde{x}}^{sym} \boldsymbol{u}^m d\Omega_{\tilde{t}}^f$$
$$+ \int_{\Omega_{\tilde{t}}^f} \nabla_{\tilde{x}} \cdot \boldsymbol{w}^m \lambda^m \nabla_{\tilde{x}} \cdot \boldsymbol{u}^m d\Omega_{\tilde{t}}^f, \qquad (18)$$

Here, $\nabla_{\tilde{x}}$ is the gradient operator on $\Omega_{\tilde{t}}$ and $\nabla_{\tilde{x}}^{sym}$ is its symmetric counterpart; μ^m and λ^m are the Lamé parameters of the fictitious elastic problem.

3.3.4 Coupled FSI problem

The variational formulation of the coupled fluid–structure interaction problem is stated as follows: Find $p_g \in \mathscr{X}_g^p$, $p_q \in \mathscr{X}_q^p$, $\boldsymbol{v}_g \in \mathscr{X}_g^v$, $\boldsymbol{v}_q \in \mathscr{X}_q^v$, $\varphi \in \mathscr{X}^\varphi$, $\Upsilon \in \mathscr{X}^\Upsilon$, $\boldsymbol{u} \in \mathscr{X}^s$ and $\boldsymbol{u}^m \in \mathscr{V}^m$ such that $\forall w_g^1 \in \mathscr{Y}_g^p$, $\boldsymbol{w}_g^2 \in \mathscr{Y}_g^v$, $w^3 \in \mathscr{Y}^\varphi$, $w^4 \in \mathscr{Y}^\Upsilon$, $\boldsymbol{w}^s \in \mathscr{Y}^s$ and $\boldsymbol{w}^m \in \mathscr{W}^m$,

$$B^f(w_g^1, \boldsymbol{w}_g^2, w^3, w^4, p_g + p_q, \boldsymbol{v}_g + \boldsymbol{v}_q, \varphi, \Upsilon; \widehat{\boldsymbol{v}}) \qquad (19)$$
$$+ B^s(\boldsymbol{w}^s, \boldsymbol{u}) + B^m(\boldsymbol{w}^m, \boldsymbol{u}^m) = F^f(\boldsymbol{w}^2) + F^s(\boldsymbol{w}^s),$$

with the following compatibility conditions at the fluid–structure interface:

$$\boldsymbol{v}_g = \frac{\partial \boldsymbol{u}}{\partial t} \circ \boldsymbol{\phi}^{-1} \quad \text{on} \quad \Gamma_t, \qquad (20a)$$

$$\boldsymbol{w}_g^2 = \boldsymbol{w}^s \circ \boldsymbol{\phi}^{-1} \quad \text{on} \quad \Gamma_t. \qquad (20b)$$

Note that Eq. (20a) imposes strongly the kinematical compatibility at the fluid–structure interface while Eq. (20b) leads to a weak enforcement of traction compatibility, i.e., $\boldsymbol{\sigma}^f \boldsymbol{n}^f + \boldsymbol{\sigma}^s \boldsymbol{n}^s = 0$ on Γ_t, where $\boldsymbol{n}^s$ is the unit outward normal to the solid boundary in the spatial configuration.

3.4 Semidiscrete formulation

We use NURBS–based isogeometric analysis for the spatial discretization of the coupled problem. Let us define finite–dimensional approximations of the funtional spaces, namely, $\mathscr{X}_h^p \subset \mathscr{X}_g^p$, $\mathscr{X}_h^v \subset \mathscr{X}_g^v$, $\mathscr{X}_h^\varphi \subset \mathscr{X}^\varphi$, $\mathscr{X}_h^\Upsilon \subset \mathscr{X}^\Upsilon$, $\mathscr{X}_h^s \subset \mathscr{X}^s$, and $\mathscr{V}_h^m \subset \mathscr{V}^m$. Analogously, we introduce $\mathscr{Y}_h^p \subset \mathscr{Y}_g^p$, $\mathscr{Y}_h^v \subset \mathscr{Y}_g^v$, $\mathscr{Y}_h^\varphi \subset \mathscr{Y}^\varphi$, $\mathscr{Y}_h^\Upsilon \subset \mathscr{Y}^\Upsilon$, $\mathscr{Y}_h^s \subset \mathscr{Y}^s$, and $\mathscr{W}_h^m \subset \mathscr{W}^m$.

Let us now use $\varphi_h \in \mathscr{X}_h^\varphi$ and the coarse–scale velocity $\boldsymbol{v}_h \in \mathscr{X}_h^v$ and pressure fields $p_h \in \mathscr{X}_h^p$ to approximate the fine scales of the velocity and pressure fields as

$$\boldsymbol{v}_q = -\frac{\tau_{SUPS}}{\rho} \boldsymbol{r}_M, \qquad (21a)$$

$$p_q = -\rho v_{LSIC} r_C. \qquad (21b)$$

Here, $\boldsymbol{r}_M$ and r_C are given by

$$\boldsymbol{r}_M = \rho \left(\frac{\partial \boldsymbol{v}_h}{\partial t} \bigg|_{\widehat{x}} + (\boldsymbol{v}_h - \widehat{\boldsymbol{v}}_h) \cdot \nabla \boldsymbol{v}_h \right) - \nabla \cdot \boldsymbol{\sigma}_h^f - \rho \boldsymbol{f}, \qquad (22a)$$

$$r_C = \nabla \cdot \boldsymbol{v}_h, \qquad (22b)$$

where $\boldsymbol{\sigma}_h^f = \bar{\mu} \left(\nabla \boldsymbol{v}_h + \nabla^T \boldsymbol{v}_h \right) - p_h \boldsymbol{I} - \gamma_f \varepsilon \nabla \varphi_h \otimes \nabla \varphi_h$. For the stabilization parameters τ_{SUPS} and v_{LSIC} we use the expressions

$$\tau_{SUPS} = \left(\frac{4}{\Delta t^2} + (\boldsymbol{v}_h - \widehat{\boldsymbol{v}}_h) \cdot \boldsymbol{G}(\boldsymbol{v}_h - \widehat{\boldsymbol{v}}_h) + C_I v^2 \boldsymbol{G} : \boldsymbol{G} \right)^{-1/2},$$
$$\qquad (23a)$$

$$v_{LSIC} = (\text{tr}(\boldsymbol{G}) \, \tau_{SUPS})^{-1}, \qquad (23b)$$

where Δt is, in a time-discrete context, the time step; $C_I = 1/12$ is a positive constant; ν is the kinematic viscosity; and $\boldsymbol{G}$ denotes the element metric tensor [6]. The stabilized formulation of the fluid problem over the finite element spaces can be stated as: Find $p_h \in \mathscr{X}_h^p$, $\boldsymbol{v}_h \in \mathscr{X}_h^v$, $\varphi_h \in \mathscr{X}_h^\varphi$ and $\Upsilon_h \in \mathscr{X}_h^\Upsilon$ such that $\forall w_h^1 \in \mathscr{Y}_h^p$, $\boldsymbol{w}_h^2 \in \mathscr{Y}_h^v$, $w_h^3 \in \mathscr{Y}_h^\varphi$ and $w_h^4 \in \mathscr{Y}_h^\Upsilon$,

$$B_{MS}^f(w_h^1, \boldsymbol{w}_h^2, w_h^3, w_h^4, p_h, \boldsymbol{v}_h, \varphi_h, \Upsilon_h; \widehat{\boldsymbol{v}}_h) = F^f(\boldsymbol{w}_h^2), \qquad (24)$$

where

$$\begin{aligned}
B_{MS}^f(w_h^1, \boldsymbol{w}_h^2, w_h^3, w_h^4, p_h, \boldsymbol{v}_h, \varphi_h, \Upsilon_h; \widehat{\boldsymbol{v}}_h) &= \int_{\Omega_t^f} w_h^1 \nabla \cdot \boldsymbol{v}_h \mathrm{d}\Omega_t^f \\
&+ \int_{\Omega_t^f} \boldsymbol{w}_h^2 \cdot \rho \left(\left. \frac{\partial \boldsymbol{v}_h}{\partial t} \right|_{\widehat{x}} + (\boldsymbol{v}_h - \widehat{\boldsymbol{v}}_h) \cdot \nabla \boldsymbol{v}_h \right) \mathrm{d}\Omega_t^f \\
&+ \int_{\Omega_t^f} \nabla \boldsymbol{w}_h^2 : \boldsymbol{\sigma}_h^f \mathrm{d}\Omega_t^f + \int_{\Omega_t^f} w_h^3 \left(\left. \frac{\partial \varphi_h}{\partial t} \right|_{\widehat{x}} + (\boldsymbol{v}_h - \widehat{\boldsymbol{v}}_h) \cdot \nabla \varphi_h \right) \mathrm{d}\Omega_t^f \\
&+ \int_{\Omega_t^f} \nabla w_h^3 \cdot M_\varphi \gamma_f \nabla \left(\frac{1}{\varepsilon} W_\varphi' - \varepsilon \Upsilon_h \right) \mathrm{d}\Omega_t^f \\
&+ \int_{\Omega_t^f} w_h^4 \Upsilon_h \mathrm{d}\Omega_t^f + \int_{\Omega_t^f} \nabla w_h^4 \cdot \nabla \varphi_h \mathrm{d}\Omega_t^f \\
&- \int_{\Gamma_t} w_h^4 |\nabla \varphi_h| \cos(\theta_c) \mathrm{d}\Gamma_t \\
&+ \sum_{e=1}^{n_{el}} \int_{\Omega_t^{f,e}} \tau_{SUPS} \left((\boldsymbol{v}_h - \widehat{\boldsymbol{v}}_h) \cdot \nabla \boldsymbol{w}_h^2 + \frac{\nabla w_h^1}{\rho} \right) \cdot \boldsymbol{r}_M \mathrm{d}\Omega_t^f \\
&+ \sum_{e=1}^{n_{el}} \int_{\Omega_t^{f,e}} \nu_{LSIC} \rho \nabla \cdot \boldsymbol{w}_h^2 r_C \mathrm{d}\Omega_t^f \\
&- \sum_{e=1}^{n_{el}} \int_{\Omega_t^{f,e}} \tau_{SUPS} \boldsymbol{w}_h^2 \cdot (\boldsymbol{r}_M \cdot \nabla \boldsymbol{v}_h) \mathrm{d}\Omega_t^f \\
&- \sum_{e=1}^{n_{el}} \int_{\Omega_t^{f,e}} \frac{\nabla \boldsymbol{w}_h^2}{\rho} : (\tau_{SUPS} \boldsymbol{r}_M \otimes \tau_{SUPS} \boldsymbol{r}_M) \mathrm{d}\Omega_t^f \\
&- \sum_{e=1}^{n_{el}} \int_{\Omega_t^{f,e}} \frac{\tau_{SUPS}}{\rho} w_h^3 \boldsymbol{r}_M \cdot \nabla \varphi_h \mathrm{d}\Omega_t^f \qquad (25)
\end{aligned}$$

Here, n_{el} is the total number of elements on the fluid mesh and $\Omega_t^{f,e}$ the region of the physical space occupied by element e at time t.

We can now approximate the coupled FSI problem (19) by the following variational formulation over the finite element spaces: Find $p_h \in \mathscr{X}_h^p$, $\boldsymbol{v}_h \in \mathscr{X}_h^v$, $\varphi_h \in \mathscr{X}_h^\varphi$, $\Upsilon_h \in \mathscr{X}_h^\Upsilon$, $\boldsymbol{u}_h \in \mathscr{X}_h^s$ and $\boldsymbol{u}_h^m \in \mathscr{V}_h^m$ such that $\forall w_h^1 \in \mathscr{Y}_h^p$, $\boldsymbol{w}_h^2 \in \mathscr{Y}_h^v$, $w_h^3 \in \mathscr{Y}_h^\varphi$, $w_h^4 \in \mathscr{Y}_h^\Upsilon$, $\boldsymbol{w}_h^s \in \mathscr{Y}_h^s$ and $\boldsymbol{w}_h^m \in \mathscr{W}_h^m$,

$$\begin{aligned}
&B_{MS}^f(w_h^1, \boldsymbol{w}_h^2, w_h^3, w_h^4, p_h, \boldsymbol{v}_h, \varphi_h, \Upsilon_h; \widehat{\boldsymbol{v}}_h) + B^s(\boldsymbol{w}_h^s, \boldsymbol{u}_h) \\
&+ B^m(\boldsymbol{w}_h^m, \boldsymbol{u}_h^m) = F^f(\boldsymbol{w}_h^2) + F^s(\boldsymbol{w}_h^s), \qquad (26)
\end{aligned}$$

where

$$p_h(\boldsymbol{x}, t) = \sum_{A \in I_f} p_A(t) N_A(\boldsymbol{x}, t), \qquad (27a)$$

$$w_h^1(\boldsymbol{x}, t) = \sum_{A \in I_f} w_A^1 N_A(\boldsymbol{x}, t), \qquad (27b)$$

$$\boldsymbol{u}_h(\boldsymbol{X}, t) = \sum_{A \in I_s} \boldsymbol{u}_A(t) \widehat{N}_A(\boldsymbol{X}), \qquad (27c)$$

$$\boldsymbol{w}_h^s(\boldsymbol{X}) = \sum_{A \in I_s} \boldsymbol{w}_A^s \widehat{N}_A(\boldsymbol{X}), \qquad (27d)$$

$$\boldsymbol{u}_h^m(\tilde{\boldsymbol{x}}, \tilde{t}) = \sum_{A \in I_f} \widehat{\boldsymbol{u}}_A(\tilde{t}) \tilde{N}_A(\tilde{\boldsymbol{x}}, \tilde{t}), \qquad (27e)$$

$$\boldsymbol{w}_h^m(\tilde{\boldsymbol{x}}, \tilde{t}) = \sum_{A \in I_f} \boldsymbol{w}_A^m \tilde{N}_A(\tilde{\boldsymbol{x}}, \tilde{t}), \qquad (27f)$$

$$\widehat{\boldsymbol{v}}_h(\boldsymbol{x}, t) = \sum_{A \in I_f} \frac{\partial \widehat{\boldsymbol{u}}_A}{\partial t}(t) N_A(\boldsymbol{x}, t). \qquad (27g)$$

The rest of the variables ($\boldsymbol{v}_h$, φ_h and Υ_h) and the weighting functions ($\boldsymbol{w}_h^2$, w_h^3 and w_h^4) are defined analogously to p_h and w_h^1, respectively. In Eqs. (27), the $\widehat{N}_A$'s are a set of basis functions defined on Ω_0 that are fixed in time. In the context of IGA, these functions are splines with controllable continuity. In the interior of the fluid and solid domains, their continuity can be arbitrarily high but on Γ_0 (in the normal direction) is exactly $\mathscr{C}^0$. I_s denotes the global–index set of the $\widehat{N}_A$'s that correspond to the solid domain. N_A is the push forward of $\widehat{N}_A$ to the spatial domain Ω_t, i.e., $N_A(\boldsymbol{x}, t) = \widehat{N}_A \circ \widehat{\boldsymbol{\phi}^h}^{-1}(\boldsymbol{x}, t)$, where $\widehat{\boldsymbol{\phi}^h}^{-1}$ is the discrete counterpart of $\widehat{\boldsymbol{\phi}}^{-1}$. Likewise, $\tilde{N}_A$ is the push forward of $\widehat{N}_A$ to the spatial domain at time $\tilde{t}$, i.e., $\tilde{N}_A(\tilde{\boldsymbol{x}}, \tilde{t}) = \widehat{N}_A \circ \widehat{\boldsymbol{\phi}^h}^{-1}(\tilde{\boldsymbol{x}}, \tilde{t})$. I_f is the global–index set of the N_A's that correspond to the fluid domain.

In order to enforce the compatibility conditions at the fluid-structure interface and taking into account that we work with matching discretizations, we define a unique set of both trial an test functions for the velocity at the fluid–structure interface. This leads to strong (pointwise) satisfaction of the kinematics condition and weak satisfaction of the traction compatibility condition.

3.5 Time discretization and numerical implementation

In this section, we present the time integration algorithm for our FSI problem. We use the generalized-α method, which was originally proposed by Chung and Hulbert [22] for the equations of structural dynamics. Subsequently, this technique was extended to the equations of fluid mechanics [39] and successfully applied to fluid-structure interaction problems (see, for instance, [3,13,15]).

3.5.1 Time stepping scheme

Let us call $\boldsymbol{U}, \dot{\boldsymbol{U}}, \ddot{\boldsymbol{U}}$ the vectors of control variable degrees of freedom of the fluid–structure system, and its first and second time derivatives, respectively. Analogously, let us call $\boldsymbol{V}, \dot{\boldsymbol{V}}, \ddot{\boldsymbol{V}}$ the vectors of control variable degrees of freedom of mesh displacements, velocities and accelerations. We define the residual vectors

$$\boldsymbol{R}^{cont} = \{R_A^{cont}\}, \tag{28a}$$

$$\boldsymbol{R}^{mom} = \{R_{A,i}^{mom}\}, \tag{28b}$$

$$\boldsymbol{R}^{\varphi} = \{R_A^{\varphi}\}, \tag{28c}$$

$$\boldsymbol{R}^{aux} = \{R_A^{aux}\}, \tag{28d}$$

$$\boldsymbol{R}^{mesh} = \{R_{A,i}^{mesh}\}, \tag{28e}$$

where A is a control–variable index and i is an index associated to the spatial dimensions. The residual components are defined as

$$R_A^{cont} = B_{MS}^f(\{N_A, 0, 0, 0\}, \{p_h, \boldsymbol{v}_h, \varphi_h, \Upsilon_h\}; \widehat{\boldsymbol{v}_h}), \tag{29a}$$

$$\begin{aligned} R_{A,i}^{mom} &= B_{MS}^f(\{0, N_A\boldsymbol{e}_i, 0, 0\}, \{p_h, \boldsymbol{v}_h, \varphi_h, \Upsilon_h\}; \widehat{\boldsymbol{v}_h}) \\ &\quad + B^s(\widehat{N_A}\boldsymbol{e}_i, \boldsymbol{u}_h) - F^s(\widehat{N_A}\boldsymbol{e}_i) - F^f(\widehat{N_A}\boldsymbol{e}_i), \end{aligned} \tag{29b}$$

$$R_A^{\varphi} = B_{MS}^f(\{0, 0, N_A, 0\}, \{p_h, \boldsymbol{v}_h, \varphi_h, \Upsilon_h\}; \widehat{\boldsymbol{v}_h}), \tag{29c}$$

$$R_A^{aux} = B_{MS}^f(\{0, 0, 0, N_A\}, \{p_h, \boldsymbol{v}_h, \varphi_h, \Upsilon_h\}; \widehat{\boldsymbol{v}_h}), \tag{29d}$$

$$R_{A,i}^{mesh} = B^m(\tilde{N}_A\boldsymbol{e}_i, \boldsymbol{u}_h^m), \tag{29e}$$

where $\boldsymbol{e}_i$ is the ith cartesian basis vector. Our time stepping scheme can be defined as follows: Given the discrete approximation to the global vectors of control variables at time t_n, namely, $\boldsymbol{U}_n, \dot{\boldsymbol{U}}_n, \ddot{\boldsymbol{U}}_n, \boldsymbol{V}_n, \dot{\boldsymbol{V}}_n, \ddot{\boldsymbol{V}}_n$ and the current time step size $\Delta t = t_{n+1} - t_n$, find $\boldsymbol{U}_{n+1}, \dot{\boldsymbol{U}}_{n+1}, \ddot{\boldsymbol{U}}_{n+1}, \boldsymbol{V}_{n+1}, \dot{\boldsymbol{V}}_{n+1}, \ddot{\boldsymbol{V}}_{n+1}$ such that

$$\boldsymbol{R}^{cont}(\boldsymbol{U}_{n+\alpha_f}, \dot{\boldsymbol{U}}_{n+\alpha_f}, \ddot{\boldsymbol{U}}_{n+\alpha_m}, \boldsymbol{V}_{n+\alpha_f}, \dot{\boldsymbol{V}}_{n+\alpha_f}, \ddot{\boldsymbol{V}}_{n+\alpha_m}) = 0, \tag{30a}$$

$$\boldsymbol{R}^{mom}(\boldsymbol{U}_{n+\alpha_f}, \dot{\boldsymbol{U}}_{n+\alpha_f}, \ddot{\boldsymbol{U}}_{n+\alpha_m}, \boldsymbol{V}_{n+\alpha_f}, \dot{\boldsymbol{V}}_{n+\alpha_f}, \ddot{\boldsymbol{V}}_{n+\alpha_m}) = 0, \tag{30b}$$

$$\boldsymbol{R}^{\varphi}(\boldsymbol{U}_{n+\alpha_f}, \dot{\boldsymbol{U}}_{n+\alpha_f}, \ddot{\boldsymbol{U}}_{n+\alpha_m}, \boldsymbol{V}_{n+\alpha_f}, \dot{\boldsymbol{V}}_{n+\alpha_f}, \ddot{\boldsymbol{V}}_{n+\alpha_m}) = 0, \tag{30c}$$

$$\boldsymbol{R}^{aux}(\boldsymbol{U}_{n+\alpha_f}, \dot{\boldsymbol{U}}_{n+\alpha_f}, \ddot{\boldsymbol{U}}_{n+\alpha_m}, \boldsymbol{V}_{n+\alpha_f}, \dot{\boldsymbol{V}}_{n+\alpha_f}, \ddot{\boldsymbol{V}}_{n+\alpha_m}) = 0, \tag{30d}$$

$$\boldsymbol{R}^{mesh}(\boldsymbol{U}_{n+\alpha_f}, \dot{\boldsymbol{U}}_{n+\alpha_f}, \ddot{\boldsymbol{U}}_{n+\alpha_m}, \boldsymbol{V}_{n+\alpha_f}, \dot{\boldsymbol{V}}_{n+\alpha_f}, \ddot{\boldsymbol{V}}_{n+\alpha_m}) = 0, \tag{30e}$$

where

$$\dot{\boldsymbol{U}}_{n+1} = \dot{\boldsymbol{U}}_n + \Delta t((1-\gamma)\ddot{\boldsymbol{U}}_n + \gamma\ddot{\boldsymbol{U}}_{n+1}), \tag{31a}$$

$$\boldsymbol{U}_{n+1} = \boldsymbol{U}_n + \Delta t\dot{\boldsymbol{U}}_n + \frac{\Delta t^2}{2}\left((1-2\beta)\ddot{\boldsymbol{U}}_n + 2\beta\ddot{\boldsymbol{U}}_{n+1}\right), \tag{31b}$$

$$\dot{\boldsymbol{V}}_{n+1} = \dot{\boldsymbol{V}}_n + \Delta t((1-\gamma)\ddot{\boldsymbol{V}}_n + \gamma\ddot{\boldsymbol{V}}_{n+1}), \tag{31c}$$

$$\boldsymbol{V}_{n+1} = \boldsymbol{V}_n + \Delta t\dot{\boldsymbol{V}}_n + \frac{\Delta t^2}{2}\left((1-2\beta)\ddot{\boldsymbol{V}}_n + 2\beta\ddot{\boldsymbol{V}}_{n+1}\right). \tag{31d}$$

The α–levels are defined as

$$\boldsymbol{U}_{n+\alpha_f} = \boldsymbol{U}_n + \alpha_f(\boldsymbol{U}_{n+1} - \boldsymbol{U}_n), \tag{32a}$$

$$\boldsymbol{U}_{n+\alpha_m} = \boldsymbol{U}_n + \alpha_m(\boldsymbol{U}_{n+1} - \boldsymbol{U}_n). \tag{32b}$$

The parameters α_f, α_m, γ and β are chosen as in [3] leading to second–order time accuracy, unconditional stability of the time–integration algorithm for linear ordinary differential equation systems with constant coefficients, and an optimally damped fluid subproblem. The nonlinear system of equations (30) is solved using a Newton–Raphson iteration procedure.

4 Numerical examples

In this section, we present a series of numerical examples that illustrate the predictive ability of our model and the effectiveness of our computational method. The first numerical example uses the NSCH equations without solid to reproduce the coalescence of two droplets. We aim to show that the radius of the meniscus formed during the coalescence process follows the scaling law observed in experimental and theoretical results. The second example demonstrates that our model can be used to simulate the deformation caused by a droplet on an underlying substrate. Our results are compared with experimental data taken from the literature. Subsequently, we present a numerical simulation of capillary origami. A droplet of glycerol is deposited on a solid membrane and the capillary forces at the interface fold the structure until the droplet is partially wrapped by the membrane. Our next example reproduces the deformation caused by capillary forces in elastic micropillars. Finally, we present a three dimensional simulation of a slender structure deformed by a wetting droplet. Note that gravity forces are negligible at small scales and, as a consequence, they are not considered in the numerical examples presented in this paper.

## 4.1 Coalescence of droplets

When two droplets come into contact, they form a bridge and coalesce due to surface tension. The NSCH model given

in Eqs. (1) can be used to study droplet coalescence for incompressible, two-component, immiscible fluids with matched density and viscosity. To solve the NSCH equations, we use the algorithm described in Section 3, annihilating all the terms corresponding to the solid mechanics and the mesh–motion subproblems. Fig. 1 shows a sequence of isocontour plots of the interface along the coalescence process of two water droplets. For simplicity, we considered a two-dimensional domain. Note that the time $t = 0.0$ does not refer to the initial time of the simulation, but to the instant when the interfaces of both droplets come into contact. Initially, the dynamics is driven by a large Laplace pressure originating from the high curvature at the contact region, where a meniscus is formed. Early in the process, the droplets retain their circular shape to some extent ($t < 0.15\,ms$). By time $t \sim 4\,ms$ the two initial droplets can be barely discerned. At this point, the dynamics starts to operate on larger time scales. The shape of the droplet evolves toward a circle that minimizes the interfacial length. However, the gradual accumulation of kinetic energy along the process produces a "rebound" effect in the shape of the droplet; see the evolution between $t \sim 8\,ms$ and $t \sim 400\,ms$. We consider that the solution at time $t = 400\,ms$ is a good approximation of the steady state.

The initial dynamics of the merger process is amenable to simplified theoretical models that provide the time evolution of the meniscus radius $r(t)$; see the bottom-right inset of Fig. 2 for a pictorial description of $r(t)$. The theoretical model [30] predicts the scaling $r(t) \sim \sqrt{t}$ for $r \gtrsim 0.03R$, where R is the droplet radius. This result is also backed up by experimental observations [1]. Fig. 2 shows the time evolution of r obtained from the simulation (red squares) and the function $g(t) = \chi\sqrt{t}$ (blue solid line), where χ is a fitting constant parameter. The diagram shows a good agreement between both datasets, demonstrating that our model reproduces correctly the initial dynamics of merging droplets.

4.2 Static wetting on soft substrates

The static equilibrium shape of a liquid droplet on a flat and rigid substrate is well understood. The droplet's shape is a spherical cap which contacts the solid with an equilibrium contact angle $\theta_E = \arccos[(\gamma_{SG} - \gamma_{SL})/\gamma_f]$ given by the Young-Dupré equation [24]. In the contact angle equation, γ_{SG} and γ_{SL} are the surface tension at the solid-gas and at the solid-liquid interface, respectively. When the solid is sufficiently compliant or the droplet sufficiently small for the elastocapillary length scale $l_{ec} = \gamma_f/E$ to be comparable to the droplet radius, Young–Dupré's equation breaks down. The excess Laplace pressure in the interior of the droplet creates a dimple in the wet area and capillary forces produce a ridge at the contact line. To show that our FSI model can successfully predict this phenomenon, we reproduce one
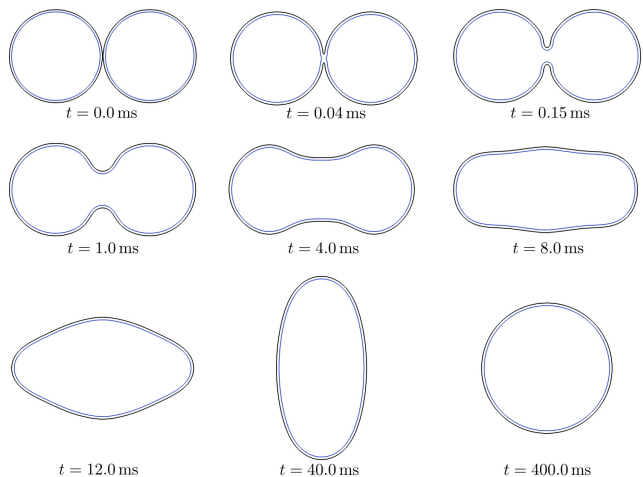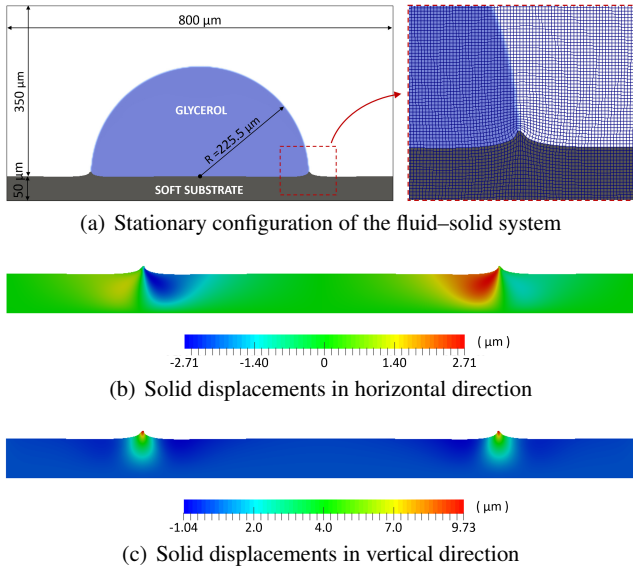

Fig. 1 Time evolution of the interface shown by isocontour lines of φ. We plot $\varphi = 0.7$ (blue) and $\varphi = -0.7$ (black). The computational domain (not shown) is $\Omega = (0, 1.5L) \times (0, L)$, where $L = 1.0\,cm$. The mesh is composed of 256×384 $\mathscr{C}^1$-quadratic elements. We imposed periodic boundary conditions in both directions. The initial configuration consisted of two water droplets of radius $R = 0.2\,cm$ centered at $(0.543L, 0.5L)$ and $(0.957L, 0.5L)$, respectively. The physical parameters correspond to water at 20°C, i.e., $\gamma_f = 72.86\,mN/m$, $\mu = 1.0\,mPa\,s$ and $\rho = 1.0\,g/cm^3$. The thickness of the interface and the mobility were set to $\varepsilon = 3.9\,10^{-3}\,cm$, and $M_\varphi = 10^{-3}\,cm^3 s/g$, respectively.
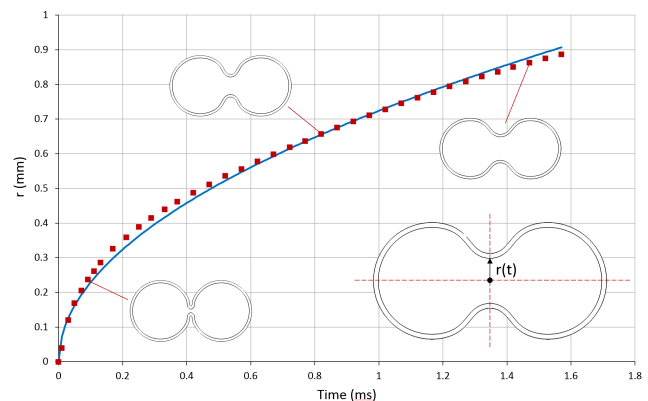
Fig. 2 Time evolution of the meniscus radius r obtained from the computation (red points) and trend line given by $g(t) = \chi\sqrt{t}$ with $\chi = 22.9$ (blue line). The initial time on the horizontal axis refers to the instant when the interfaces of both droplets come into contact.
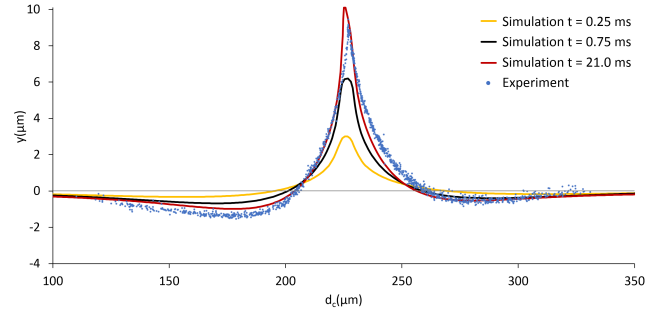
of the experiments reported in [57]. In particular, a glycerol droplet of radius $R = 225.5\,\mu m$ is deposited on a soft substrate with Young's modulus $E = 3.0\,kPa$. The droplet deforms the substrate as shown on the left–hand side of Fig. 3(a). The contact angle θ_c in the boundary condition (5) is given by $\theta_E = \arccos[(\gamma_{SG} - \gamma_{SL})/\gamma_f]$, but the solid deformation produces an apparent contact angle (measured with respect to a horizontal line) that is smaller than θ_E. In simple words, the droplet "sinks" in the substrate and looks "more wetting" that it would do on a rigid surface. The right–hand side of Fig. 3(a) portraits a detailed view of the contact line

(a) Stationary configuration of the fluid–solid system

(b) Solid displacements in horizontal direction

(c) Solid displacements in vertical direction

Fig. 3 Glycerol droplet deposited on a soft substrate. (a) Stationary configuration (left) and detail of the contact line region after deformation (right). (b), (c) solid displacements in the horizontal and vertical directions, respectively. We use a uniform mesh of 400×200 quadratic elements. On the left, right and lower boundaries of the computational domain, we impose zero velocity in the normal direction. On the upper boundary, zero velocity is imposed in both directions. We adopted the values of surface tension reported in [57], i.e., $\gamma_f = 46.0\,m\mathrm{N/m}$, $\gamma_{SA} = 31\,m\mathrm{N/m}$ and $\gamma_{SL} = 36\,m\mathrm{N/m}$. For the viscosity and density parameters, we use values for glycerol: $\mu = 1412.0\,m\mathrm{Pa\,s}$ and $\rho = 1.26\,pg/\mu\mathrm{m}^3$. We took $\varepsilon = 2.0\,\mu\mathrm{m}$ and $M_\varphi = 0.1\,\mu\mathrm{m}^3\mu\mathrm{s}/pg$. The parameters for the solid correspond to a silicone gel with $E = 3.0\,k\mathrm{Pa}$, $\nu^s = 0.499$ and $\rho^s = 12.6\,pg/\mu\mathrm{m}^3$.

neighborhood and also shows the mesh in the current configuration. It may be observed that the fictitious linear elasticity problem used to move the fluid domain produces a smooth transition of the element shape using the solid displacement at the fluid–solid interface as boundary condition. Figs. 3(b) and 3(c) show, respectively, the substrate's displacements in the horizontal and vertical directions, when equilibrium is reached.

To perform a more quantitative analysis, we measured the displacement of the fluid–solid interface close to the contact line and we compared our results with the experimental data reported in [57]; see Fig. 4. The experimental results are available only for the stationary configuration (blue dots). Our computational method enables us to understand the dynamics of the process. We report the solution at times $t = 0.25\,m\mathrm{s}$ (yellow), $t = 0.75\,m\mathrm{s}$ (purple) and $t = 21.0\,m\mathrm{s}$ (red), when we considered the solution to be stationary. Note that our model neglects the disjoining pressure. At the length scales considered in this paper, the disjoining pressure is expected to have an impact only close to the contact line. Based on the results presented in Fig. 4, the impact of the disjoining pressure on the global deformation seems to be small, which justifies our assumption.

Fig. 4 Vertical displacements of the fluid–solid interface. d_c in the horizontal axis represents the distance to the center of the droplet. The blue circles are the experimental measurements reported in [57], which represent a stationary configuration. The computational results are reported at $t = 0.25\,m\mathrm{s}$ (yellow), $t = 0.75\,m\mathrm{s}$ (purple) and $t = 21.0\,m\mathrm{s}$ (red), when the solution is considered to be stationary. The horizontal line $y = 0$ corresponds to the fluid–solid interface before deformation.

4.3 Capillary origami

A droplet deposited on an elastic membrane will pull the solid through surface tension. If the membrane is sufficiently compliant, the drop will fold it, giving rise to a capillary origami [49]. This process has triggered significant interest because it can be used for self-assembly of micro- and nano-structures. We use our theory to simulate the spontaneous wrapping of glycerol droplets with elastic membranes. The experiments in [49] were performed by placing the membrane on a rigid surface. Modeling this system in its entirety would require the use of contact algorithms. It is also very likely that we would need to remesh the fluid domain due to changes in its topology. To avoid this, we simply placed the membrane in the fluid omitting the underlying rigid surface; see Fig 5(a). Since we are neglecting gravity forces, we expect this simplified system to behave similarly to the capillary origamis formed on top of a rigid surface. Another difference with the experiments in [49] is that we do not consider the evaporation of the droplet. As shown in [49], a capillary origami can be produced without evaporation, but the complete encapsulation of the droplet is harder to achieve without reducing the droplet's volume.

We place a semicircular droplet of radius $R = 146.0\,\mu\mathrm{m}$ on an elastic membrane [see Fig. 5(a) for the setup of the problem] and we impose different contact angles θ_c along the fluid–structure interface. The membrane is modeled as a 3D solid. Figs. 5(b)–5(d) show how the membrane folds wrapping a droplet with contact angle $\theta_c = 90°$. After the droplet is deposited, the membrane bends downwards due to the internal Laplace pressure. Later, the ends of the membrane move upwards until the droplet gets almost fully encapsulated. Fig. 6 shows the solid mesh in the current configuration and the streamlines at time $t = 0.045\,s$. The fluid–fluid interface is drawn as a black solid line. The flow inside

the droplet is predominantly vertical. Outside the droplet, the membrane's motion produces well-defined vortices.

Fig. 7 shows the influence of the contact angle on the dynamics of the process. The initial conditions are the same as before. The results suggest that droplet encapsulation occurs faster for more wetting fluids. This observation can be used to have better control in the process of self-assembly of micro- and nano-structures.

4.4 Wetting of elastic micropillars

Wetting of fibrous media has been widely studied due to its importance in natural and engineered systems. However, most of the research focuses on rigid fibers. At small scales, capillary forces outweigh bulk forces and deform fibers significantly, which produces a coupled problem combining elasticity and wetting [29]. Here, we use our FSI model to study quantitatively the deformation of micropillars produced by a fluid–fluid interface. Fig. 8(a) shows the setup of our problem. We place a small amount of liquid (blue) between the two micropillars (grey) and let capillary forces deform the fibers. The micropillars are clamped at the bottom by preventing the displacements in horizontal and vertical directions. Fig. 8(b) shows how surface tension deforms the fibers bringing them close to each other, which, in turn, produces the rise of the liquid.

We observe that, in addition to the obvious parameters controlling the dynamics (the geometry and the mechanical properties of the fibers as well as the physical properties of the fluid) the volume of liquid placed between the micropillars plays a key role. We quantified the volume using the height of the liquid column as shown in Fig. 8; see the plots on the left-hand side. The top, middle and bottom rows correspond, respectively, to $h = 200.0\,\mu$m, $h = 300.0\,\mu$m and $h = 400.0\,\mu$m. It may be observed that for a given geometrical configuration of the fibers, larger volumes of liquid produce larger deformations. In addition, the dynamics of the process seems to be faster for larger volumes of liquid. This might be explained as follows: Capillary forces have a constant magnitude across all examples, but act at different points of the micropillars due to the different location of the interface. The torque applied to the micropillars is larger for larger volumes, producing stronger deformations. In addition, capillary forces are always oriented at an angle θ_c, owing to the boundary condition given by Eq. (5)(a). Since capillary forces act as follower loads, they have a larger vertical component as the micropillars deform.
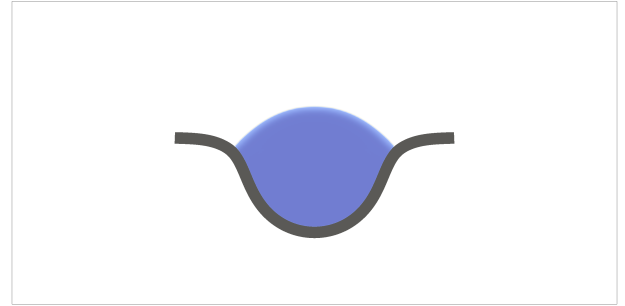
4.5 Three dimensional wrapping of a liquid droplet

Here, we study the three dimensional wrapping of a liquid droplet with an elastic membrane. Fig. 9(a) shows the initial
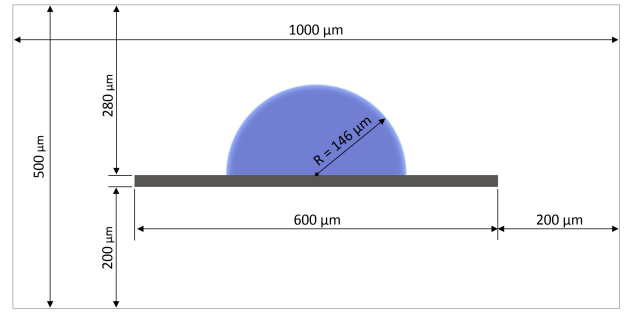
(a) $\theta_c = 90°, t = 0.0\,$s
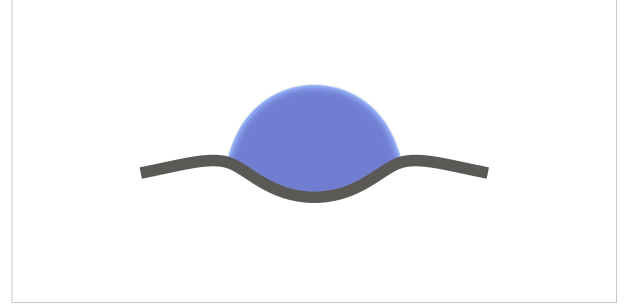
(b) $\theta_c = 90°, t = 0.014\,$s

(c) $\theta_c = 90°, t = 0.075\,$s

(d) $\theta_c = 90°, t = 0.138\,$s

Fig. 5 Capillary origami. (a) Initial condition. A semicircular droplet (blue) is deposited on an elastic membrane (grey). (b), (c) and (d) Current configuration at $t = 0.014\,$s, $t = 0.075\,$s and $t = 0.138\,$s, respectively. We use a uniform mesh of 200×100 quadratic elements. We impose zero velocity in normal direction on all boundaries. The parameters employed in this computation for the fluid correspond to a glycerol droplet, in particular, $\mu = 1412.0\,m$Pa s, $\gamma_f = 46.0\,m$N/m, and $\rho = 1.26\,pg/\mu$m^3. We take $\varepsilon = 5.0\,\mu$m and $M_\varphi = 0.1\,\mu$m$^3\mu$s$/p$g. For the elastic membrane we adopt $E = 30.0\,k$Pa, $v^s = 0.45$, and $\rho^s = 12.6\,pg/\mu$m^3.

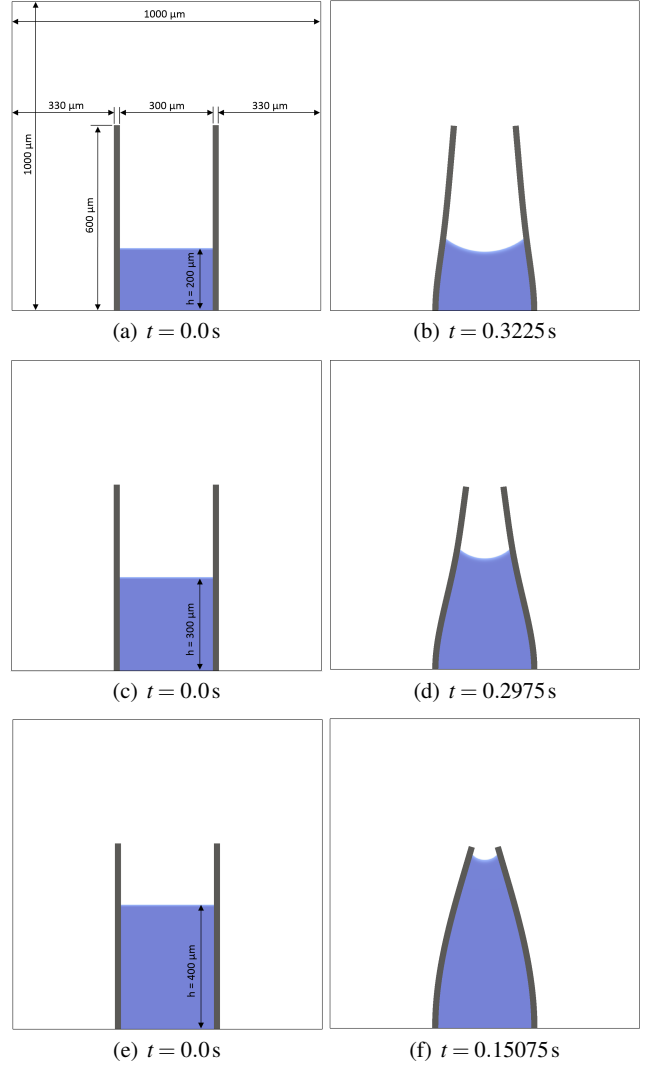Velocity Magnitude 0.0 0.81 1.62 2.43 3.24 (mm/s)
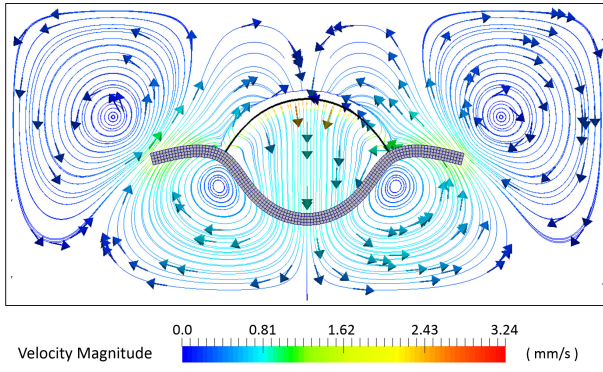
Fig. 6 Solid mesh and streamlines of the fluid velocity at time $t = 0.045\,$s for the capillary origami of Fig. 5. The arrows show the direction of the velocity field. The streamlines and the arrows are colored with the velocity magnitude. The interface of the droplet is represented by a black, solid line.

(a) $\theta_c = 60°, t = 0.065\,$s

(b) $\theta_c = 120°, t = 0.302\,$s
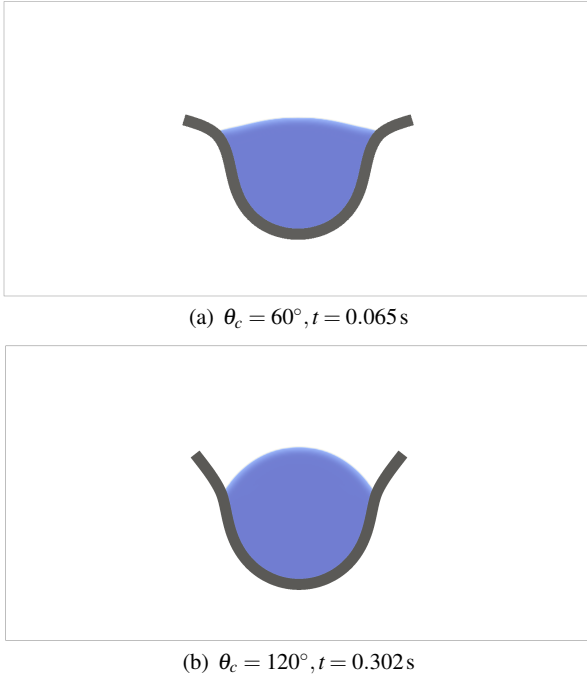
Fig. 7 Capillary origami for two different contact angles. (a) Wetting droplet at time $t = 0.065\,$s. (b) Non–wetting droplet at time $t = 0.302\,$s.

(a) $t = 0.0\,$s

(b) $t = 0.3225\,$s

(c) $t = 0.0\,$s

(d) $t = 0.2975\,$s

(e) $t = 0.0\,$s

(f) $t = 0.15075\,$s

Fig. 8 Wetting of elastic micropillars. The top, middle and bottom row correspond, respectively, to $h = 200.0\,\mu$m, $h = 300.0\,\mu$m and $h = 400.0\,\mu$m. We impose zero velocity in normal direction on all the boundaries, except on the upper one, where we only enforce a stress–free condition. We use a wetting liquid with contact angle $\theta_c = 60°$. The parameters are $\mu = 1412.0\,m$Pa s, $\gamma_f = 46.0\,m$N/m, $\varepsilon = 2.5\,\mu$m, $\rho = 1.26\,p$g$/\mu$m^3, $M_\varphi = 0.1\,\mu$m$^3\mu$s$/p$g, $E = 320.0\,k$Pa, $v^s = 0.45$ and $\rho^s = 12.6\,p$g$/\mu$m^3.

configuration of the problem, which consists of a droplet of radius $R = 146.0\,\mu$m (blue) deposited on a membrane of thickness $20.0\,\mu$m (grey) that covers an entire horizontal plane of the computational domain. The elastic membrane is clamped to the lateral boundaries, where we have prevented the displacements in normal and vertical directions. We carry out this simulation assuming that the droplet is a wetting liquid that forms a contact angle of $\theta_c = 60°$ with the solid membrane. The left panels in Fig. 9 show an upper view of the problem. The right panels are vertically flipped, so that we can easily observe the membrane's deformation. The surface tension at the interface folds the solid, resulting

in the partial wrapping of the droplet [see Fig. 9(b)]. The initial square shape of the elastic membrane leads to a non–axisymmetric deformation of the structure and triggers the formation of wrinkles [Fig. 9(c)]. Different values of surface tension and solid stiffness should result in different patterns of the wrinkling instability [20, 36].

5 Conclusions

We have proposed a computational method for three–dimensional, dynamic simulation of elastocapillarity. The solid dynamics is governed by the equations of nonlinear elastodynamics

(a) $t = 0.0\,$s

(b) $t = 0.00625\,$s

(c) $t = 0.125\,$s
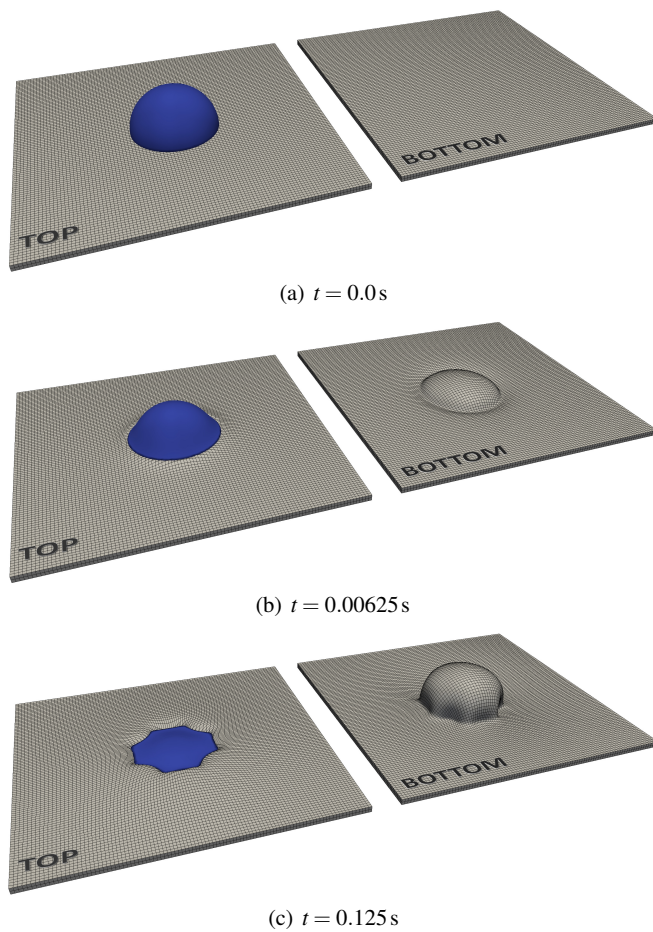
Fig. 9 Top view (left panels) and bottom view (right panels) of the three dimensional wrapping of a liquid droplet. (a) A hemispherical droplet is deposited on a elastic membrane that is clamped to the lateral boundaries of the computational domain. (b) Capillary forces fold the membrane and lead to the partial wrapping of the liquid droplet. (c) A wrinkling instability is developed on the structure, triggered by the non–axisymmetric shape of the membrane. Note that we are only representing the solid domain and one of the fluid phases. The computational domain (not shown) is $\Omega = (0,L) \times (0,L) \times (0,0.5L)$, where $L = 1$ mm. We used a uniform mesh with $100 \times 100 \times 50$ quadratic elements. We impose zero velocity in normal direction on all the boundaries as well as zero vertical velocity on the lateral boundaries. The parameters correspond to a glycerol droplet: $\mu = 1412.0\,m$Pa s, $\gamma_f = 46.0\,m$N/m, $\rho = 1.26\,pg/\mu$m^3. We take $\varepsilon = 10.0\,\mu$m and $M_\varphi = 0.1\,\mu$m$^3,\mu$s$/pg$. For the membrane we employ $E = 0.6\,k$Pa, $v^s = 0.45$, and $\rho^s = 12.6\,pg/\mu$m^3.

in the Lagrangian description. The fluid theory models the dynamics of two-component, immiscible fluids with surface tension. We adopt a fully–implicit fluid–structure interaction algorithm to solve the problem. We use a boundary–fitted method with the fluid equations written in Arbitrary Lagrangian–Eulerian coordinates. The motion of the mesh is described by the equations of elastostatics. We have shown the viability of our theoretical framework and numerical algorithm by solving several examples of elastocapillary phenomena in two and three dimensions. This work is expected

to open new avenues in the study of elastocapillarity. For example, we believe that it would be interesting to study capillary origamis with a model that accounts for evaporation of the droplet. This can be accomplished by using a fluid theory that allows for liquid-vapor phase transformations, such as, the Navier–Stokes–Korteweg equations [13]. Our framework can also be extended to model capillary fracture [10]. This can be accomplished by coupling the current model with a fracture theory.

References

1. D. G. A. L. Aarts, H. N. W. Lekkerkerker, H. Guo, G. H. Wegdam, and D. Bonn. Hydrodynamics of droplet coalescence. *Phys. Rev. Lett.*, 95:164503, 2005.
2. Y. Bazilevs, V.M. Calo, J.A. Cottrell, J.A. Evans, T.J.R. Hughes, S. Lipton, M.A. Scott, and T.W. Sederberg. Isogeometric Analysis using T-splines. *Computer Methods in Applied Mechanics and Engineering*, 199(58):229 – 263, 2010.
3. Y. Bazilevs, V.M. Calo, T.J.R. Hughes, and Y. Zhang. Isogeometric Fluid-Structure Interaction: Theory, algorithms, and computations. *Computational Mechanics*, 43(1):3–37, 2008.
4. Y. Bazilevs, M.-C. Hsu, and M.A. Scott. Isogeometric fluid-structure interaction analysis with emphasis on non-matching discretizations, and with application to wind turbines. *Computer Methods in Applied Mechanics and Engineering*, 249-252:28–41, 2012.
5. Y. Bazilevs, K. Takizawa, T. E. Tezduyar, M.-C. Hsu, N. Kostov, and S. McIntyre. Aerodynamic and fsi analysis of wind turbines with the ale-vms and st-vms methods. *Archives of Computational Methods in Engineering*, 21(4):359–398, 2014.
6. Y. Bazilevs, K. Takizawa, and T.E. Tezduyar. *Computational Fluid-Structure Interaction. Methods and Applications*. Wiley, 2013.
7. Y. Bazilevs, K. Takizawa, T.E. Tezduyar, M.-C. Hsu, N. Kostov, and S. McIntyre. Aerodynamic and FSI Analysis of Wind Turbines with the ALE-VMS and ST-VMS Methods. *Archives of Computational Methods in Engineering*, 21(4):359–398, 2014.
8. L. Beirao da Veiga, A. Buffa, G. Sangalli, and R. Vazquez. Analysis suitable T-splines of arbitrary degree: Definition, linear independence, and approximation properties. *Mathematical Models and Methods in Applied Sciences*, 23(11):1979–2003, 2013.
9. J. Bico, B. Roman, L. Moulin, and A. Boudaoud. Adhesion: elastocapillary coalescence in wet hair. *Nature*, 432(7018):690–690, 2004.
10. J. B. Bostwick and K. E. Daniels. Capillary fracture of soft gels. *Physical Review E*, 88(4):042410, 2013.
11. C. E. Brennen. *Fundamentals of multiphase flow*. Cambridge university press, 2005.
12. J. Bueno, Y. Bazilevs, R. Juanes, and H. Gomez. Droplet motion driven by tensotaxis. *Extreme Mechanics Letters*, 13:10 – 16, 2017.
13. J. Bueno, C. Bona-Casas, Y. Bazilevs, and H. Gomez. Interaction of complex fluids and solids: Theory, algorithms and application to phase-change-driven implosion. *Computational Mechanics*, 55(6):1105–1118, 2015.

14. J. Bueno and H. Gomez. Liquid-vapor transformations with surfactants. phase-field model and isogeometric analysis. *Journal of Computational Physics*, 321:797 – 818, 2016.

15. H. Casquero, C. Bona-Casas, and H. Gomez. A NURBS-based immersed methodology for fluid-structure interaction. *Computer Methods in Applied Mechanics and Engineering*, 284:943–970, 2015.

16. H. Casquero, C. Bona-Casas, and H. Gomez. NURBS-based numerical proxies for red blood cells and circulating tumor cells in microscale blood flow. *Computer Methods in Applied Mechanics and Engineering*, 316:646 – 667, 2017. Special Issue on Isogeometric Analysis: Progress and Challenges.

17. H. Casquero, L. Lei, J. Zhang, A. Reali, and H. Gomez. Isogometric collocation using analysis-suitable T-splines of arbitrary degree. *Computer Methods in Applied Mechanics and Engineering*, 301:164 – 186, 2016.

18. H. Casquero, L. Lei, Y. Zhang, A. Reali, J. Kiendl, and H. Gomez. Arbitrary-degree T-splines for isogeometric analysis of fully nonlinear Kirchhoff-Love shells. *Computer-Aided Design*, 82:140 – 153, 2017.

19. H. Casquero, L. Liu, C. Bona-Casas, Y. Zhang, and H. Gomez. A hybrid variational-collocation immersed method for fluid-structure interaction using unstructured T-splines. *International Journal for Numerical Methods in Engineering*, 105(11):855–880, 2016.

20. E. Cerda and L. Mahadevan. Geometry and physics of wrinkling. *Physical review letters*, 90(7):074302, 2003.

21. N. Chakrapani, B. Wei, A. Carrillo, P. M. Ajayan, and R. S. Kane. Capillarity-driven assembly of two-dimensional cellular carbon nanotube foams. *Proceedings of the National Academy of Sciences*, 101(12):4009–4012, 2004.

22. J. Chung and G.M. Hulbert. A time integration algorithm for structural dynamics with improved numerical dissipation: The generalized-α method. *Journal of Applied Mechanics*, 60:371–375, 1993.

23. J. Austin Cottrell, Thomas J. R. Hughes, and Yuri Bazilevs. *Isogeometric Analysis Toward Integration of CAD and FEA*. Wiley, 2009.

24. P. G. de Gennes. Wetting: statics and dynamics. *Reviews of Modern Physics*, 57:827–863, 1985.

25. M. DeVolder and A. J. Hart. Engineering hierarchical nanostructures by elastocapillary self-assembly. *Angewandte Chemie International Edition*, 52(9):2412–2425, 2013.

26. J. Donea and A. Huerta. *Finite Element Methods for Flow Problems*. Wiley, 2003.

27. J. Donea, A. Huerta, J.-Ph. Ponthot, and A. Rodrguez-Ferran. *Encyclopedia of Computational Mechanics. Arbitrary Lagrangian-Eulerian Methods.*, volume 1, chapter 14. John Wiley & Sons, Ltd, 2004.

28. C. Duprat, A. D. Bick, P. B. Warren, and H. A. Stone. Evaporation of drops on two parallel fibers: Influence of the liquid morphology and fiber elasticity. *Langmuir*, 29(25):7857–7863, 2013. PMID: 23705986.

29. C. Duprat, S. Protiere, A. Y. Beebe, and H. A. Stone. Wetting of flexible fibre arrays. *Nature*, 482(7386):510–513, 2012.

30. J. Eggers, J. R. Lister, and H. A. Stone. Coalescence of liquid drops. *Journal of Fluid Mechanics*, 401:293–310, 1999.

31. H. Gomez, V.M. Calo, Y. Bazilevs, and T.J.R. Hughes. Isogeometric Analysis of the Cahn-Hilliard phase-field model. *Computer Methods in Applied Mechanics and Engineering*, 197:43334352, 2008.

32. H. Gomez and T.J.R. Hughes. Provably unconditionally stable, second-order time-accurate, mixed variational methods for phase-field models. *Journal of Computational Physics*, 230(13):5310–5327, 2011.

33. H. Gomez, A. Reali, and G. Sangalli. Accurate, efficient, and (iso) geometrically flexible collocation methods for phase-field models. *Journal of Computational Physics*, 262:153–171, 2014.

34. H. Gomez and K. van der Zee. *Encyclopedia of Computational Mechanics. Computational phase-field modeling.* John Wiley & Sons, Ltd, 2016.

35. M.-C. Hsu, I. Akkerman, and Y. Bazilevs. Finite element simulation of wind turbine aerodynamics: validation study using nrel phase vi experiment. *Wind Energy*, 17(3):461–481, 2014.

36. J. Huang, M. Juszkiewicz, W. H. de Jeu, E. Cerda, T. Emrick, N. Menon, and T. P. Russell. Capillary wrinkling of floating thin polymer films. *Science*, 317(5838):650–653, 2007.

37. T.J.R. Hughes, J.A. Cottrell, and Y. Bazilevs. Isogeometric Analysis: CAD, Finite Elements, NURBS, exact geometry and mesh refinement. *Computer Methods in Applied Mechanics and Engineering*, 194(39-41):4135 – 4195, 2005.

38. T.J.R. Hughes, W.K. Liu, and T.K. Zimmermann. Lagrangian-Eulerian Finite Element formulation for incompressible viscous flows. *Computer Methods in Applied Mechanics and Engineering*, 29(3):329 – 349, 1981.

39. K.E. Jansen, C.H. Whiting, and G.M. Hulbert. A generalized-α method for integrating the filtered Navier-Stokes equations with a stabilized Finite Element Method. *Computer Methods in Applied Mechanics and Engineering*, 190(34):305 – 319, 2000.

40. J.H. Jeong, N. Goldenfeld, and J.A. Dantzig. Phase field model for three-dimensional dendritic growth with fluid flow. *Physical Review E*, 64:041602, 2001.

41. A.A. Johnson and T.E. Tezduyar. Mesh update strategies in parallel finite element computations of flow problems with moving boundaries and interfaces. *Computer Methods in Applied Mechanics and Engineering*, 119:73–94, 1994.

42. D. Kamensky, M.-C. Hsu, Schillinger D., J. A. Evans, Aggarwal A., Bazilevs Y., M. S. Sacks, and T.J.R. Hughes. An immersogeometric variational framework for fluid-structure interaction: Application to bioprosthetic heart valves. *Computer Methods in Applied Mechanics and Engineering*, 284:1005–1053, 2015.

43. D. Kamensky, M.-C. Hsu, Y. Yu, J. A. Evans, M. S. Sacks, and T.J.R. Hughes. Immersogeometric cardiovascular fluid–structure interaction analysis with divergence-conforming b-splines. *Computer Methods in Applied Mechanics and Engineering*, 314:408–472, 2017.

44. R.J. King. Pulmonary surfactant. *Journal of Applied Physiology*, 53(1):1–8, 1982.

45. J. Liu, C. M. Landis, H. Gomez, and T.J.R. Hughes. Liquid–vapor phase transition: Thermomechanical theory, entropy stable numerical formulation, and boiling simulations. *Computer Methods in Applied Mechanics and Engineering*, 297:476–553, 2015.

46. G. Lorenzo, M. A. Scott, K. Tew, T.J.R. Hughes, Y. J. Zhang, L. Liu, G. Vilanova, and H. Gomez. Tissue-scale, personalized modeling and simulation of prostate cancer growth. *Proceedings of the National Academy of Sciences*, page 201615791, 2016.

47. A. Moure and H. Gomez. Computational model for amoeboid motion: Coupling membrane and cytosol dynamics. *Physical Review E*, 94(4):042423, 2016.

48. A. Prosperetti and G. Tryggvason. *Computational methods for multiphase flow*. Cambridge university press, 2009.

49. C. Py, P. Reverdy, L. Doppler, J. Bico, B. Roman, and C. N. Baroud. Capillary origami: Spontaneous wrapping of a droplet with an elastic sheet. *Phys. Rev. Lett.*, 98:156103, Apr 2007.

50. O. Raccurt, F. Tardif, F. A. d'Avitaya, and T. Vareine. Influence of liquid surface tension on stiction of soi mems. *Journal of Micromechanics and Microengineering*, 14(7):1083, 2004.

51. B. Roman and J. Bico. Elasto-capillarity: deforming an elastic structure with a liquid droplet. *Journal of Physics: Condensed Matter*, 22(49):493101, 2010.

52. D. Shao, H. Levine, and W-J. Rappel. Coupling actin flow, adhesion, and morphology in a computational cell motility model. *Proceedings of the National Academy of Sciences*, 109(18):6851–6856, 2012.

53. J.-F. Sigrist. *Fluid-Structure Interaction*. John Wiley & Sons, Ltd, 2015.

54. J.C. Simo and T.J.R. Hughes. *Computational Inelasticity*. Springer-Verlag, New Yoirk, 1998.

55. K. Stein, R. Benney, V. Kalro, T. E. Tezduyar, J. Leonard, and M. Accorsi. Parachute fluid–structure interactions: 3-D computation. *Computer Methods in Applied Mechanics and Engineering*, 190(3):373–386, 2000.

56. K. Stein, T. Tezduyar, and R. Benney. Mesh moving techniques for fluid–structure interactions with large displacements. *Journal of Applied Mechanics*, 70:58–63, 2003.

57. R. W. Style, R. Boltyanskiy, Y. Che, J. S. Wettlaufer, L. A. Wilen, and E. R. Dufresne. Universal deformation of soft substrates near a contact line and the direct measurement of solid surface stresses. *Physical Review Letters*, 110:066103, Feb 2013.

58. R. W. Style, A. Jagota, C.-Y. Hui, and E. R. Dufresne. Elastocapillarity: Surface tension and the mechanics of soft solids. *arXiv preprint arXiv:1604.02052*, 2016.

59. K. Takizawa. Computational engineering analysis with the new-generation space–time methods. *Computational Mechanics*, 54:193–211, 2014.

60. K. Takizawa, Y. Bazilevs, and T.E. Tezduyar. Space-Time and ALE-VMS techniques for patient-specific cardiovascular Fluid-Structure Interaction modeling. *Archives of Computational Methods in Engineering*, 19(2):171–225, 2012.

61. K. Takizawa, Y. Bazilevs, T.E. Tezduyar, C.C. Long, A.L. Marsden, and K. Schjodt. ST and ALE-VMS methods for patient-specific cardiovascular fluid mechanics modeling. *Mathematical Models and Methods in Applied Sciences*, 24:2437–2486, 2014.

62. K. Takizawa, T. E. Tezduyar, T. Terahara, and T. Sasaki. Heart valve flow computation with the integrated space–time vms, slip interface, topology change and isogeometric discretization methods. *Computers & Fluids*, 2016.

63. T. Tanaka, M. Morigami, and N. Atoda. Mechanism of resist pattern collapse during development process. *Japanese journal of applied physics*, 32(12S):6059, 1993.

64. M. Taroni and D. Vella. Multiple equilibria in a simple elastocapillary system. *Journal of Fluid Mechanics*, 712:273–294, 12 2012.

65. S. H. Tawfick, J. Bico, and S. Barcelo. Three-dimensional lithography by elasto-capillary engineering of filamentary materials. *MRS Bulletin*, 41(02):108–114, 2016.

66. T.E. Tezduyar. Finite element methods for flow problems with moving boundaries and interfaces. *Archives of Computational Methods in Engineering*, 8:83–130, 2001.

67. T.E. Tezduyar, S. Aliabadi, M. Behr, A. Johnson, and S. Mittal. Parallel finite-element computation of 3D flows. *Computer*, 26(10):27–36, 1993.

68. T.E. Tezduyar and S. Sathe. Modeling of fluid–structure interactions with the space–time finite elements: Solution techniques. *International Journal for Numerical Methods in Fluids*, 54:855–900, 2007.

69. R. D. M. Travasso, E. C. Poiré, M. Castro, J. C. Rodrguez-Manzaneque, and A. Hernández-Machado. Tumor angiogenesis and vascular patterning: a mathematical model. *PloS one*, 6(5):e19989, 2011.

70. K. Vahidkhah, P. Balogh, and P. Bagchi. Flow of red blood cells in stenosed microvessels. *Scientific Reports*, 6, 2016.

71. G. Vilanova, I. Colominas, and H. Gomez. A mathematical model of tumour angiogenesis: growth, regression and regrowth. *Journal of The Royal Society Interface*, 14(126), 2017.

72. X. Wei, Y. J. Zhang, T. J. R. Hughes, and M. A. Scott. Truncated hierarchical catmull–clark subdivision with local refinement. *Computer Methods in Applied Mechanics and Engineering*, 291:1–20, 2015.

73. X. Wei, Y. J. Zhang, T. J. R. Hughes, and M. A. Scott. Extended truncated hierarchical catmull–clark subdivision. *Computer Methods in Applied Mechanics and Engineering*, 299:316–336, 2016.

74. J. Xu, G. Vilanova, and H. Gomez. Full-scale, three-dimensional simulation of early-stage tumor growth: The onset of malignancy. *Computer Methods in Applied Mechanics and Engineering*, 314:126–146, 2017.

75. L. Zhang, A. Gerstenberger, X. Wang, and W. K. Liu. Immersed finite element method. *Computer Methods in Applied Mechanics and Engineering*, 193(21):2051–2067, 2004.